Physics of Fluids

RESEARCH ARTICLE | MARCH 04 2025

Dynamics of non-Newtonian agarose gel droplet formation in two-phase microfluidic systems

Sagar N. Agnihotri ; Pradipta Kr. Das ; Femke Tolboom; Gabriel Werr ; Estelle Palierse ; Cecilia Persson ; Maria Tenje

Check for updates

Physics of Fluids 37, 032010 (2025)
https://doi.org/10.1063/5.0255319

View Online
Export Citation

Articles You May Be Interested In

Dynamics of free-surface mutually perpendicular twin liquid sheets and their atomization characteristics

Physics of Fluids (August 2019)

Numerical Modelling of the Poiseuille Flow in the Microchannel Using the Boltzmann Equation

AIP Conference Proceedings (May 2011)

26 March 2025 12:29:22

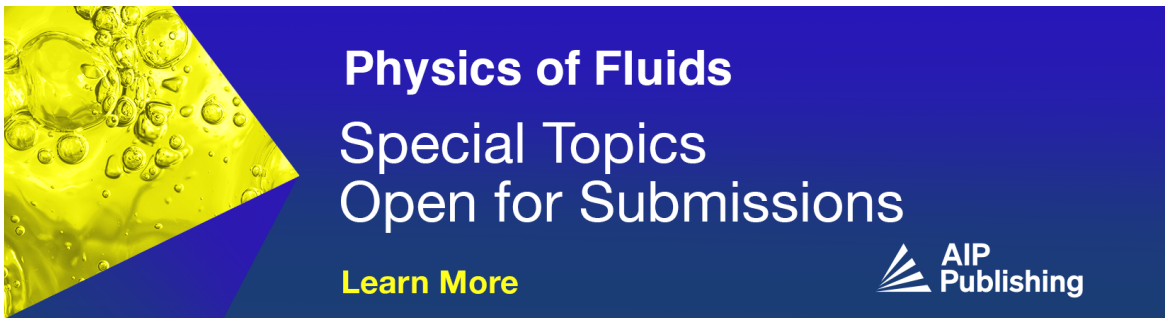

AIP Publishing

Dynamics of non-Newtonian agarose gel droplet formation in two-phase microfluidic systems

Cite as: Phys. Fluids **37**, 032010 (2025); doi: 10.1063/5.0255319
Submitted: 28 December 2024 · Accepted: 8 February 2025 ·
Published Online: 4 March 2025

View Online Export Citation CrossMark

Sagar N. Agnihotri,[1,2] Pradipta Kr. Das,[1,2] Femke Tolboom,[1,2] Gabriel Werr,[1,2] Estelle Palierse,[1] Cecilia Persson,[1] and Maria Tenje[1,2,a)]

AFFILIATIONS

[1]Division of Biomedical Engineering, Department of Materials Science and Engineering, Uppsala University, Uppsala, Sweden
[2]Science for Life Laboratory, Uppsala University, Uppsala, Sweden

[a)]Author to whom correspondence should be addressed: maria.tenje@angstrom.uu.se

ABSTRACT

Droplet-based microfluidics is a valuable tool in interdisciplinary research fields like cell biology and diagnostics. Newtonian fluids, like aqueous-based solutions, are commonly used for droplet generation. However, non-Newtonian fluids, e.g., hydrogels, are becoming increasingly popular as the dispersed phase. In this study, we investigate the dynamics of non-Newtonian ultra-low-gelling agarose droplet formation under different conditions to evaluate stability, with an aim to better understand the underlying physics of droplet formation. We varied the agarose gel concentration, temperature (40, 50, and 60 °C), and the flow rate ratio (ϕ) between the continuous and dispersed phase and observed droplet formation dynamics in the squeezing regime (capillary number, $Ca_c < 0.015$) in a T-junction under different flow conditions. We experimentally investigated the droplet size (L_D/w) as a function of those four parameters and found that L_D/w depends strongly on ϕ, the agarose concentration, and temperature (which affects the viscosity ratio, λ), but is only weakly dependent on Ca_c. We then confirmed our experimental findings with numerical simulations, which showed good agreement across all conditions. We numerically showed that the agarose droplet formation process consists of five stages, namely, filling, necking, pinching, threading, and breakup, where threading is an additional stage with a non-Newtonian dispersed phase. Finally, with numerical simulation, we concluded that threading length (l_{thread}) is directly proportional to ϕ and has a complex relation with agarose concentration, and temperature.

© 2025 Author(s). All article content, except where otherwise noted, is licensed under a Creative Commons Attribution-NonCommercial 4.0 International (CC BY-NC) license (https://creativecommons.org/licenses/by-nc/4.0/). https://doi.org/10.1063/5.0255319

26 March 2025 12:29:22

I. INTRODUCTION

Droplet-based microfluidics is a subfield within microfluidics that focuses on the controlled generation,[1,2] splitting,[3–6] merging,[7,8] trapping,[9,10] and analysis of isolated fluid droplets (dispersed phase) within a continuous, immiscible phase, usually oil. These droplets, typically ranging in volume from nanoliters (nl) to femtoliters (fl), can be precisely controlled by varying the channel geometry, fluid properties, and the flow rates of the continuous and dispersed phases.[11] The ability to have individual droplets without cross-contamination makes droplet-based microfluidics an ideal "test tube" for interdisciplinary applications, ranging from single-cell analysis,[12] cell interaction studies,[9] and particle manipulation[13] to diagnostic assays.[14] By enabling high-throughput screening, droplet microfluidics has created new opportunities for research in biology[15,16] and chemistry[17] at *nL* to *fL* scale.[18]

The most commonly used geometries for droplet generation in a two-phase microfluidic system include T-junction,[11] Y-junction,[19] flow-focusing,[20] and co-flowing devices.[21] The two immiscible phases interact at a junction in these geometries to continuously produce monodispersed droplets. Beyond these passive methods, droplet generation can also be achieved through active techniques, where external sources of energy in addition to channel geometry and flow properties, such as electric,[22] acoustic,[23,24] or magnetic fields,[25] are used to control droplet generation.[2] The droplet generation process can be classified into three regimes, namely, squeezing, dripping, and jetting—each defined by the forces involved in achieving the droplet generation.[11,26] In the squeezing regime, pressure build-up across the interface upstream and downstream is the dominant factor in overcoming surface tension forces to produce a droplet [Capillary number $Ca < 0.015$ (Ref. 26)] In the dripping regime, pressure build-up and shear stress are critical in overcoming surface tension forces to generate droplets ($Ca > 0.015$). Conversely, in the jetting regime, the dispersed phase flows parallel to the continuous phase downstream from the junction, generating droplets farther away. The physics of the jetting regime, however, remains less explored.

© Author(s) 2025

Several studies have explored the physics of droplet generation when both the continuous and dispersed phases are Newtonian,[27] i.e., where both fluids exhibit a linear relationship between shear stress and shear rate. In contrast, when one or both phases are non-Newtonian, the relationship between shear stress and shear rate is not linear, resulting in complex rheological behavior that varies with the shear rate. Non-Newtonian fluids can be classified as shear-thinning, shear-thickening, Bingham plastics, viscoelastic, and thixotropic.[28,29] Given the interdisciplinary nature of droplet microfluidics, there is an increasing application of non-Newtonian gels as dispersed phases in cell culture,[30] chemical analysis,[31] drug testing,[32,33] single-cell analysis,[34] and tissue engineering.[35] Common examples of these non-Newtonian gels include agarose,[36] alginate,[37] polyacrylamide,[38] GelMA,[39] PEG,[40] and collagen.[41] Consequently, there is a need to investigate the physics of these systems in droplet-based microfluidics to characterize the regimes and stability of droplet generation under varying flow conditions, temperatures, and gel viscosities as the physics of droplet generation involving non-Newtonian phases is far less explored compared to that of Newtonian fluids.

Chiarello *et al.*[42] investigated the dynamics of droplet formation using a shear-thinning xanthan solution and concluded that droplet size depends on the effective *Ca*, calculated by taking into consideration the shear-dependent viscosity of the xanthan solution. Similarly, Cao *et al.*[43] numerically studied droplet formation with sodium alginate as a shear-thinning solution in flow-focusing devices, demonstrating that *Ca* influences the transition from the dripping to jetting regime, which is crucial for monodisperse droplet production. Du *et al.*[44] found that the dynamics of shear-thinning fluids in flow-focusing devices closely resemble those of Newtonian fluids and experimentally investigated the rheological properties of the shear-thinning fluid and flow conditions to study the dynamics of droplet generation. Rostami and Morini,[45] in their study of Newtonian and non-Newtonian droplets, observed that the transition from the squeezing to the dripping regime is influenced by the *Ca* of the continuous phase. Khater *et al.*[46] used non-Newtonian agar gel as a dispersed phase and concluded that droplet size and regime depend on *Ca*, flow rate ratio, and agar concentration. Connecting results from earlier literatures, we realized that specifically non-Newtonian agarose gel droplet generation against different flow and thermal conditions in squeezing regime is not explored in detailed way. Given that ultra-low-gelling agarose is one of the most commonly used gels for interdisciplinary research applications as a dispersed phase and its properties are highly sensitive to thermal conditions, we selected ultra-low-gelling agarose for this study, investigating it through both experimental and numerical approaches.

In this study, we used both experimental and numerical approaches to investigate the dynamics of droplet generation in non-Newtonian ultra-low-gelling agarose gel. Specifically, within the squeezing regime, aiming to understand how factors such as gel concentration, flow rate ratio, temperature, viscosity ratio, and the underlying mechanisms influence droplet size and stability during generation. We specifically focused on the squeezing regime since, in droplet microfluidics, the squeezing regime ($Ca_c < 0.015$) generates uniform and stable droplets. To examine the role of agar concentration, we selected two concentrations, 0.5% and 2%, to assess how varying gel viscosities impact the droplet formation process. Additionally, we tested each concentration at three different temperatures, 40, 50, and 60 °C, to capture the effects of temperature on agarose viscosity and gelling properties. By carefully varying the flow conditions within the squeezing regime, we evaluated how the flow rate ratio (ϕ) and viscosity ratio (λ) between the continuous and dispersed phases affect the droplet generation dynamics experimentally. We compared our numerical model with the experimental results, and they were found to be in good agreement. Later, we used our numerical model to investigate the dynamics of agarose gel droplet formation. Our results provide insights into the stability and consistency of droplets across a range of conditions, offering valuable information for applications involving non-Newtonian gels, where factors like concentration and temperature are critical for maintaining droplet stability. Through this approach, we aim to expand the understanding of droplet generation dynamics in non-Newtonian systems, laying the groundwork for improved design and control in microfluidic applications that utilize agarose and similar biocompatible gels.

II. MATERIALS AND METHODS

A. Microfluidic device design, fabrication, and experimental setup

The microfluidic device is designed for the generation of ultra-low-gelling agarose droplets. It consists of two main sections: a standard T-junction for droplet formation, placed on a hot plate (maintained at 40, 50, or 60 °C depending on the experimental condition), and a storage/cross-linking section on a Peltier cooler set to 10 °C. The device has two inlets: one for the continuous phase, consisting of light mineral oil (Sigma-Aldrich, USA) with 2% PGPR (polyglycerol polyricinoleate, Danisco) as surfactant, and another inlet for the dispersed phase, which is ultra-low-gelling agarose hydrogel (Sigma-Aldrich) in phosphate-buffered saline (PBS) solution. The agarose concentration is either 0.5% or 2% by weight in PBS.

The continuous phase inlet channel has a width of 160 μm, while the dispersed phase inlet channel is 80 μm wide, with both channels having a height of 150 μm. The device's master mold was fabricated using an ASIGA 3D printer MAX X27. A 10:1 PDMS (polydimethylsiloxane) base-to-curing-agent mix (Sylgard 184) was poured on the mold and cured at 60 °C for 2 h. After curing, the PDMS replica was punched with a 0.75 mm tool (Welltec) and bonded to a glass slide (epredia) using a plasma oven (Diener Electronic, Germany) with 1 min of air-plasma treatment. A pressure pump (Elveflow OB1 MK4) was used to drive both phases, with the dispersed phase kept in an Eppendorf tube on a heating block at 40, 50, or 60 °C, depending on the experimental setup, as shown in Fig. 1.

B. Preparation of ultra-low-gelling agarose hydrogel

To prepare agarose gel, ultra-low-gelling point agarose powder (A5030, Sigma-Aldrich, USA) was weighed into an Eppendorf tube, and the required amount of PBS was added based on the agarose concentration required. The mixture was allowed to swell at room temperature for 45 min and then mixed briefly with a vortex mixer. It was then heated in a 70 °C heating block for an hour, with mixing every 10 min for complete solubility of agarose powder in PBS. The gel's clarity was checked to confirm homogeneity: a clear appearance indicated complete dissolution, while a cloudy look with undissolved particles suggested incomplete mixing. For immediate use, the heating block was set to 40 °C to cool the gel to this temperature. For later use, the gel was stored at 4 °C and reheated to 60 °C when needed.

26 March 2025 12:29:22

© Author(s) 2025

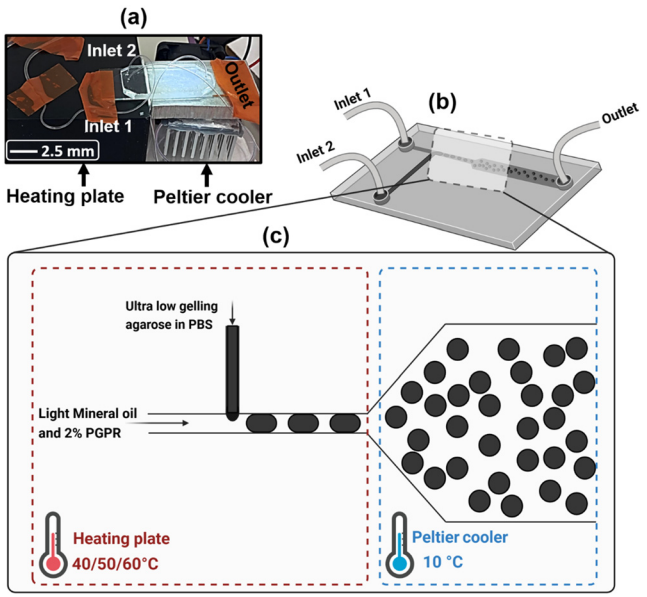

FIG. 1. Experimental setup for non-Newtonian agarose gel droplet formation in a two-phase microfluidic system. (a) Image of the actual setup, highlighting the microfluidic chip with inlet tubing for the continuous and dispersed phases, the outlet, heating plate, and Peltier cooler to facilitate agarose gel cross-linking. (b) and (c) Schematics illustrating the experimental setup components and flow design.

C. Measurement of rheological properties

The viscosity of ultra-low-gelling point agarose gel in PBS and light mineral oil with 2% PGPR was measured with flow sweep measurements on a Rheometer H10 (Discovery Series, TA Instruments), using a 20-mm-diameter geometry and Peltier plate, with 500 μm gap. The temperature was kept at 40, 50, or 60 °C, and the shear rate varied from 0.1 to 1000 s^{-1}. All the samples were kept at 40 °C before measurements. 300 μl was loaded for the agarose gels and 250 μl for the oil. Silicone oil AR 20 (Sigma-Aldrich) was applied around the sample, to avoid evaporation during experiments. All measurements were performed in triplicate. All the plots of viscosity against the shear rate are provided in supplementary material in Fig. S1. The agarose gel's viscosity vs shear rate was fitted into power law dependency to obtain consistency index (μ_{d0}) and power law index (n) for each temperature and agarose concentration and are provided in supplementary material Tables S1 and S2.

D. Data processing

A stereo microscope (Olympus, SZ61-TR) with a digital camera (Sony Exmor, CMOS) was used to record videos of each experiment. These videos were processed in ImageJ to measure droplet length (L_D), channel width (w), and speed of droplets. The dimensionless size of the droplet was calculated by taking the ratio of L_D/w. The frame rate of the video was calculated by dividing the total number of frames recorded in the video by the total time of the video and found to be in the range of 100–200 frames per second (fps). For better control of agarose flow, we used a pressure control system (Elveflow OB1 MK4) and converted pressure values to specific flow rates for the continuous (Q_c) and dispersed (Q_d) phases. The flow rate of the dispersed phases was calculated using the total volume of the droplet generated and the frequency of droplet generation, while the flow rate of the continuous phase was calculated by subtracting the flow rate of the dispersed phase from the total flow rate. The flow rate ratio was calculated as $\phi = \frac{Q_d}{Q_c}$, and since the disperse phase is non-Newtonian and follows a power-law dependency, we calculated the viscosity ratio (λ) as $\lambda = \frac{\mu_{d0}}{\mu_c}$, where μ_{d0} is the consistency index of the dispersed phase and μ_c is the viscosity of the continuous phase. The corresponding Capillary number (Ca_c) of the continuous phase was calculated as $Ca_c = \frac{\mu_c \times V_c}{\sigma}$, where V_c *and* σ represent the velocity of the continuous phase and the surface tension between the continuous and discontinuous phase.

E. Numerical setup

A three-dimensional T-junction microchannel with dimensions as shown in Fig. 2(a) is considered to investigate the dynamics of the droplet generation. Due to symmetry, only half ($y \leq 0$) of the physical domain is simulated. We have considered both the continuous and the dispersed phases to be incompressible. The governing equations for the two-phase flow are given by

$$\nabla . \mathbf{u} = 0, \tag{1}$$

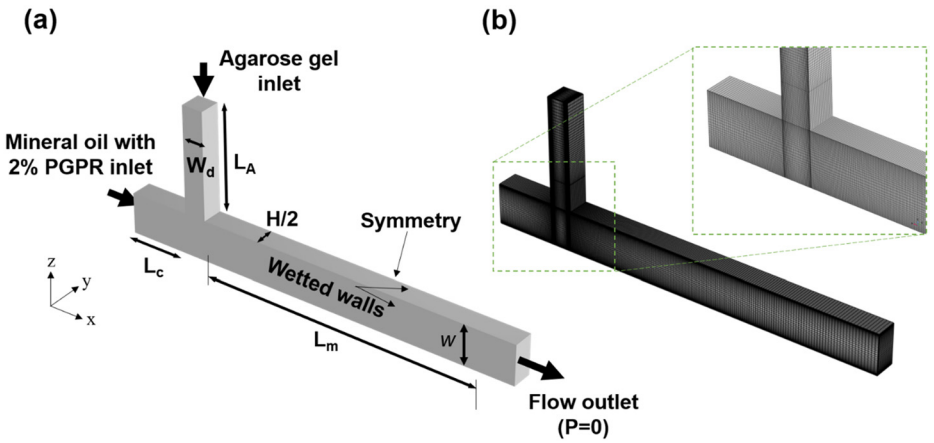

FIG. 2. Schematic of the computational setup and mesh for the study. (a) Illustration of the computational model, including boundary conditions at the oil and agarose inlets, outlet, channel walls, and symmetry planes, with L, W, and H representing the channel's length, width, and height. (b) Mesh configuration used in the computational analysis, with a zoomed view detailing the mesh structure at the T-junction.

26 March 2025 12:29:22

© Author(s) 2025

$$\rho\left[\frac{\partial \mathbf{u}}{\partial t}+(\mathbf{u}.\nabla)\mathbf{u}\right]=-\nabla p+\nabla.\boldsymbol{\tau}+\mathbf{F}_{st}, \tag{2}$$

where ρ, $\mathbf{u}$, p, $\boldsymbol{\tau}$, and $\mathbf{F}_{st}$ are density, velocity vector, pressure, viscous stress tensor, and interfacial force, respectively. The viscous stress tensor $\boldsymbol{\tau}$ is given by $\boldsymbol{\tau}=\mu\dot{\gamma}$, where μ is the viscosity and $\dot{\gamma}=\nabla\mathbf{u}+\nabla\mathbf{u}^T$ is the shear rate. To track the interface, the level set method is used as it has shown very stable and accurate interface-capturing capabilities.[47–50] We have considered a conservative level set approach to ensure that the volume bound by the interface is conserved (i.e., velocity is divergence-free). The level set function φ takes a value of 0 for one phase and 1 for the other phase. The function follows a smooth transition from 0 to 1 across the interface with $\varphi=0.5$ representing the interface. The interfacial force at the oil–gel interface is given by

$$\mathbf{F}_{st}=\sigma\kappa\delta\mathbf{n}, \tag{3}$$

where σ is the surface tension, $\kappa=-\nabla.\mathbf{n}$ is the curvature, and $\mathbf{n}=\frac{\nabla\varphi}{|\nabla\varphi|}\big|_{\varphi=0.5}$ is the outward unit normal vector at the interface. δ is the Dirac delta function and its value is zero everywhere except at the interface.

The density and the viscosity of the fluid also vary smoothly across the interface as

$$\rho=\rho_d+(\rho_c-\rho_d)\varphi, \tag{4}$$

$$\mu=\mu_d+(\mu_c-\mu_d)\varphi. \tag{5}$$

Here, $\varphi=0$ and $\varphi=1$ represent properties of agarose gel (subscript d) and oil (subscript c), respectively. The level set function is obtained by solving the following equation:

$$\frac{\partial\varphi}{\partial t}+\nabla.(\mathbf{u}\varphi)=\alpha\nabla.\left(\chi\nabla\varphi-\varphi(1-\varphi)\frac{\nabla\varphi}{|\nabla\varphi|}\right), \tag{6}$$

where α is the reinitialization parameter and χ is the parameter controlling the interface thickness. Note here, the right-hand side of Eq. (6) should ideally be zero and it is only used for numerical stability. In our present study, χ is taken as half of the maximum mesh size and α is taken as the maximum value of the velocity magnitude. We modeled the oil phase as a Newtonian fluid, whereas the agarose gel was modeled as a non-Newtonian power-law fluid. Therefore, oil phase viscosity (μ_c) does not depend on shear rate and is constant at a specific temperature. On the other hand, gel phase viscosity is expressed as $\mu_d=\mu_{d0}(\dot{\gamma})^{n-1}$, where μ_{d0} is the agarose gel flow consistency index and n is the power-law index.

The above specified governing equations are solved using the following boundary conditions: (i) at agarose gel inlet ($\varphi=0$), average gel flow velocity is specified, (ii) at mineral oil with 2% PGPR inlet ($\varphi=1$), average oil phase velocity is specified (iii) at flow outlet, zero pressure is prescribed and $\left(\chi\nabla\varphi-\varphi(1-\varphi)\frac{\nabla\varphi}{|\nabla\varphi|}\right).\mathbf{n}=0$, (iv) at y = 0, symmetry boundary condition is used, and (v) at all other boundaries, wetted wall having contact angle 135° is specified.

The governing equations along with the specified boundary conditions are solved using COMSOL Multiphysics 6.1, where we consider $W_d=80\ \mu$m , $W=150\ \mu$m , $H=160\ \mu$m , $L_m=1200\ \mu$m , $L_c=220\ \mu$m , $L_A=400\ \mu$m , and $\rho_c=838.4$ kg/m^3. A constant surface tension of $\sigma=14$ mN/m[51] has been considered throughout the study, as earlier works[46,52] indicate that the interfacial tension between light oil and agarose gel shows negligible variation across agarose concentrations of 0.5%–2% and temperatures ranging from 40 to 60 °C. For 0.5% agarose gel concentration, dispersed phase density has been taken as $\rho_d=950.87$,[46] whereas for a concentration of 2.0%, it is taken as $\rho_d=1003.2$ kg/m^3. The viscosities of the oil and gel phases show a strong temperature dependence, and their values are obtained from the rheological measurement data (see Fig. S1).

It is well established that the accuracy and efficiency of numerical solutions are strongly influenced by the mesh sizes used in the numerical studies. While smaller mesh sizes yield more accurate solutions, they also significantly increase computational demands. Therefore, an optimal mesh is selected through a mesh independence study, balancing accuracy, and computational cost. In this study, quadrilateral meshes were utilized, where rectangular meshes were initially generated on one side (on the $y=0$ plane) with a maximum element size $\Delta h_{\max}$, and a mesh sweep was performed along the y direction, discretizing half the channel depth into equally sized elements. Four computational meshes (i.e., M1–M4) were generated by gradually increasing the number of elements from 34 000 to 387 000. The droplet size (L_D/w) was subsequently estimated for 0.5% and 2.0% agarose solutions at 40 and 60 °C under flow rate ratios of 0.1 and 1, as summarized in Tables I and II. A comparative analysis revealed that the mesh M3 comprising of 288 000 elements and $\Delta h_{\max}=1.2\ \mu$m yielded results with a relative error less than 0.2%. Based on this high-level accuracy, we used this mesh for all the simulations reported in the study. The time step (Δt) employed in this study has been carefully determined based on the estimation of the Courant number, which is defined as: $C=\frac{\Delta t\, U_{\max}}{\Delta h_{\max}}$, where $U_{\max}$ represents the maximum fluid velocity within the domain. To ensure numerical stability and accuracy, the Courant number must satisfy the condition $C<1$.

III. RESULTS AND DISCUSSION

A. Effect of temperature and flow rate ratio (ϕ)

In this section, we investigated the effect of temperature on the droplet size (L_D/w). In the first set of experiments, we maintained the agarose concentration constant and varied the temperature from 40 to 60 °C for different values of Ca_c and ϕ. We plotted this effect of temperature in Fig. 3, where L_D/w is plotted on the left-hand side of the Y axis against Ca_c on the X axis and ϕ on the right-hand side of the Y axis. Below each plot, representative images from the experimental conditions illustrate the droplet formation at each temperature.

At 40 °C, Fig. 3(a) indicates that lower ϕ correspond to smaller values of L_D/w, suggesting that the fluid dynamics in the squeezing regime are strongly governed by ϕ, with weak to negligible dependence on Ca_c. Figures 3(b) and 3(c) further illustrate this relationship, showing droplet images obtained at $\phi=0.91$ and $\phi=0.68$ resulting in

TABLE I. Mesh convergence analysis: effect of mesh size on droplet size (L_D/w) for 0.5% agarose solutions at 40 and 60 °C.

Mesh number	No. of elements	$\Delta h_{\max}$ (μm)	40 °C		60 °C	
			$\phi=0.1$	$\phi=1.0$	$\phi=0.1$	$\phi=1.0$
M1	34 000	2.4	1.475	2.525	1.90	1.97
M2	117 000	1.6	1.502	2.42	1.89	2.77
M3	288 000	1.2	1.511	2.415	1.880	2.753
M4	387 000	1.1	1.512	2.41	1.878	2.750

26 March 2025 12:29:22

© Author(s) 2025

TABLE II. Mesh convergence analysis: effect of mesh size on droplet size (L_D/w) for 2.0% agarose solutions at 40 and 60 °C.

			40 °C		60 °C	
Mesh number	No. of elements	Δh_{max} (μm)	$\phi = 0.1$	$\phi = 1.0$	$\phi = 0.1$	$\phi = 1.0$
M1	34 000	2.4	1.35	No breakup	1.446	3.085
M2	117 000	1.6	1.370	3.06	1.485	3.22
M3	288 000	1.2	1.375	3.08	1.488	3.29
M4	387 000	1.1	1.376	3.09	1.49	3.295

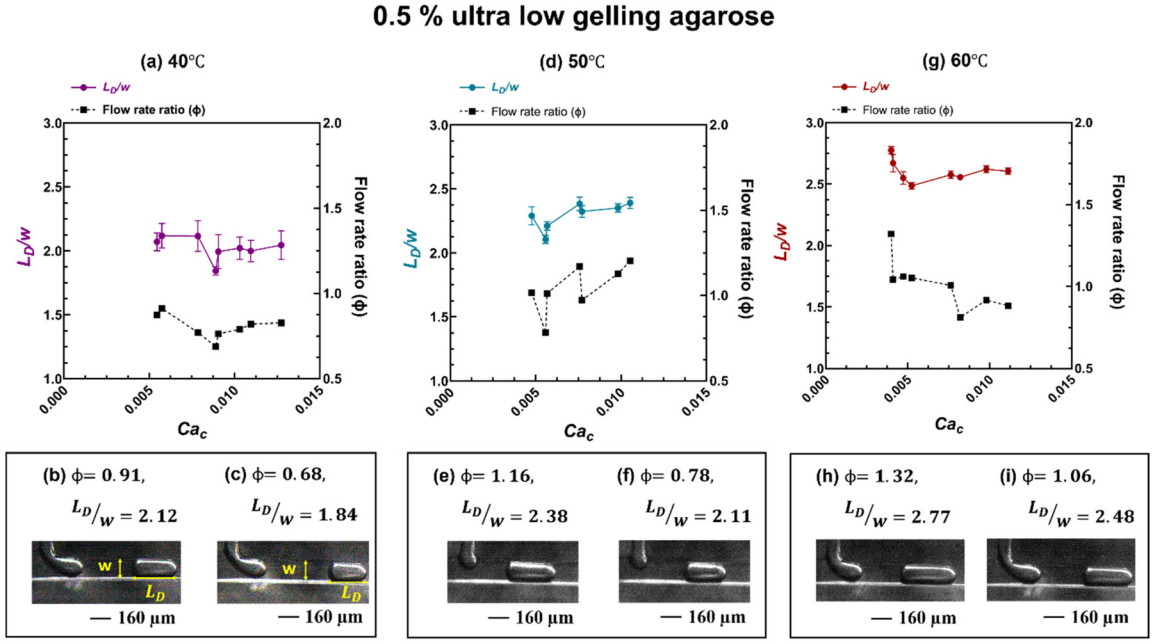

FIG. 3. Effect of temperature (40, 50, and 60 °C) on 0.5% agarose gel concentration on droplet generation in the squeezing regime, studied experimentally. (a), (d), and (g) Plots of dimensionless droplet size (L_D/w) on the left Y axis and flow rate ratio (ϕ) on the right Y axis, against the capillary number of the continuous phase (Ca_c) on the X axis. (b) and (c) Images at 40 °C with $\phi = 0.91$ and $\phi = 0.68$, resulting in (L_D/w) values of 2.12 and 1.84, respectively. (e) and (f) Images at 50 °C with $\phi = 1.16$ and $\phi = 0.78$, resulting in (L_D/w) values of 2.38 and 2.11. (h) and (i) Images at 60 °C with $\phi = 1.32$ and $\phi = 1.06$, resulting in (L_D/w) values of 2.77 and 2.48.

L_D/w of 2.12 and 1.84, respectively. As the temperature increases to 50 °C, as depicted in Fig. 3(d), we observe that the L_D/w values continue to rise compared to those at 40 °C. Figures 3(e) and 3(f) showcase images corresponding to $\phi = 1.16$ and 0.78, yielding larger droplet sizes, with measured L_D/w values of 2.38 and 2.11. This upward trend persists at 60 °C, illustrated in Fig. 3(g), where Figs. 3(i) and 3(j) present images from experiments at $\phi = 1.32$ and 1.06 leading to the largest observed droplet sizes of 2.77 and 2.48. The experimental results reveal the interplay between ϕ, temperature, and Ca_c on L_D/w. Operating within the squeezing regime, we observed that Ca_c has minimal to no impact on L_D/w, whereas ϕ and temperature have a significant influence on the size of the droplet formed.

Similar trends were observed for droplet generation with 2% agarose gel concentration at the same temperatures. At 40 °C [Fig. 4(a)], we observe that lower ϕ values result in smaller droplet size (L_D/w), but the droplets were unstable with high variability, indicating that this regime is unsuitable for producing monodisperse droplets. Figures 4(b) and 4(c) show droplets formed at $\phi = 0.1065$ and $\phi = 0.018$, with L_D/w values of 1.44 and 1.26, respectively. At 50 °C [Fig. 4(d)], the L_D/w values increase relative to those at 40 °C. Figures 4(e) and 4(f) show droplets at $\phi = 0.23$ and $\phi = 0.1365$, yielding larger droplets with L_D/w values of 1.59 and 1.43. Under these conditions, droplets formed at $Ca_c < 0.007$ remain unstable, exhibiting a large standard deviation. This upward trend in L_D/w continues at 60 °C, as seen in Fig. 4(g), with Figs. 4(i) and 4(j) showing droplets produced at $\phi = 0.549$ and $\phi = 0.1425$, leading to the largest observed droplet sizes of 2.16 and 1.66. At this temperature, droplets are monodispersed and stable.

In summary, for both 0.5% and 2% agarose concentrations, droplet size (L_D/w) demonstrates a strong dependence on both ϕ and temperature, while Ca_c has minimal impact within the squeezing regime. Droplets formed at 60 °C are monodisperse and stable, whereas those at 40 and 50 °C exhibit higher variability and instability.

To examine the combined effects of agarose concentration and temperature, we plotted the dimensionless droplet size L_D/w against ϕ

26 March 2025 12:29:22

© Author(s) 2025

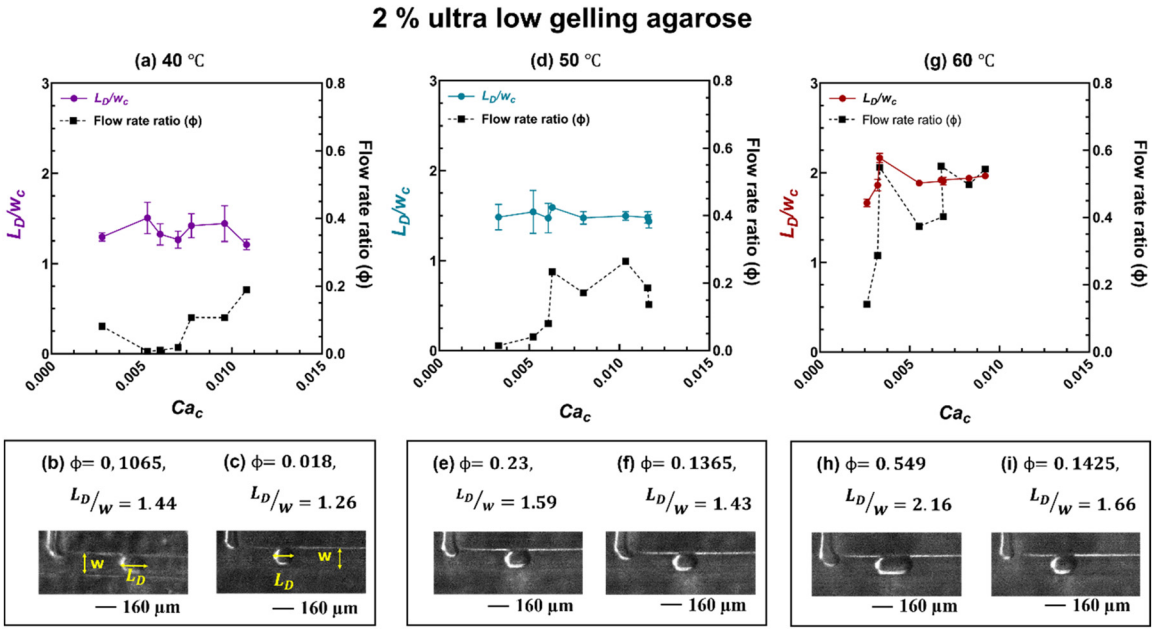

FIG. 4. Effect of 2% agarose gel concentration and temperatures (40, 50, and 60 °C) on droplet generation in the squeezing regime, studied experimentally. (a), (d), and (g) Plots of dimensionless droplet size (L_D/w) on the left Y axis and flow rate ratio (ϕ) on the right Y axis, against the capillary number of the continuous phase (Ca_c) on the X axis. (b) and (c) Images at 40 °C with $\phi = 0.1065$ and $\phi = 0.018$, resulting in (L_D/w) values of 1.44 and 1.26, respectively. (e) and (f) Images at 50 °C with $\phi = 0.23$ and $\phi = 0.1365$, resulting in (L_D/w) values of 1.59 and 1.43. (h) and (i) Images at 60 °C with $\phi = 0.549$ and $\phi = 0.1425$, resulting in (L_D/w) values of 2.16 and 1.66.

in all the experimental conditions to see how these two parameters are linked together [see Fig. 5(a)]. We observed that, with ϕ, L_D/w increases linearly. Hence to understand the effect of other parameters experimentally, we used the ratio $[(L_d/w)/\phi]$ against temperature and agarose concentration. We have plotted the overall $[(L_d/w)/\phi]$ obtained across different concentrations (0.5% and 2%) and temperature conditions (40, 50, and 60 °C), regardless of Ca_c (since Ca_c has minimum influence on droplet size in squeezing regime), as discussed in previous sections and shown in Figs. 5(b) and 5(c). We observed that an increase in temperature has a complex rheological effect on $[(L_D/w)/\phi]$ for 0.5% and 2% agarose concentrations. An increase in temperature decreases the viscosity of both oil and agarose gel, while the increase in agarose concentration increases the viscosity of only the dispersed phase. Considering this effect, we experimentally observed that, overall, for 0.5% agarose, the ratio of $[(L_D/w)/\phi]$ is maximum at 60 °C and minimum at 50 °C, while for 2% agarose gel, this ratio is maximum at 40 °C and minimum at 60 °C. However, due to the high standard deviation at 40 and 50 °C along with the unstable droplet production in this condition, it is difficult to experimentally conclude the exact effect and we therefore performed numerical studies to

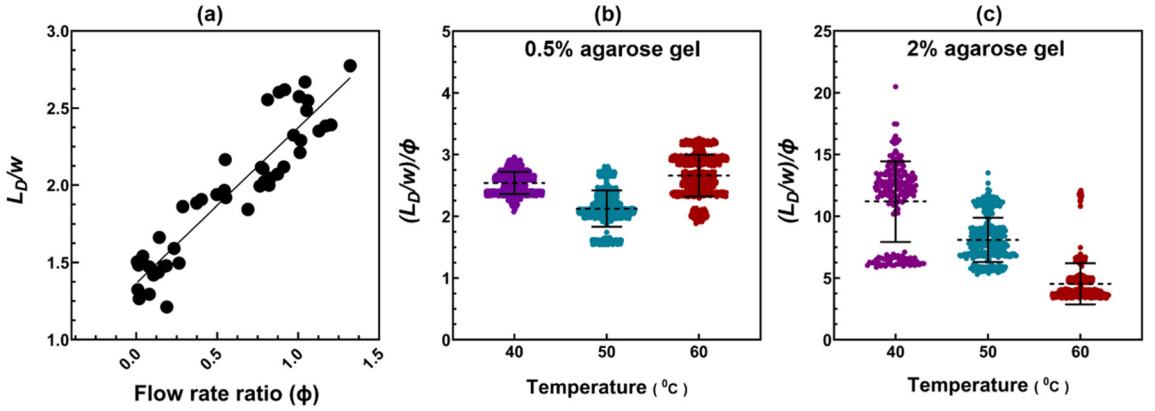

FIG. 5. (a) Plot illustrating the effect of flow rate ratio (ϕ) on dimensionless droplet size (L_D/w) involving all the experimental values. (b) Plot illustrating the effect of temperature (40, 50, and 60 °C) on the ratio of dimensionless size per flow rate ratio $[(L_D/w)/\phi]$ with concentrations of 0.5% agarose studied experimentally. (c) Plot illustrating the effect of temperature (40, 50, and 60 °C) on the ratio of dimensionless size per flow rate ratio $[(L_D/w)/\phi]$ with concentrations of 2% agarose studied experimentally.

26 March 2025 12:29:22

© Author(s) 2025

understand this effect deeper. Droplet generation with 0.5% agarose is stable and uniform across all the temperatures tested compared to 2% agarose concentration.

B. Numerical study on dynamics of agarose gel droplet formation

1. Comparison of numerical study with experiments

We compared experimental and numerical results for the generation of ultra-low-gelling agarose droplets across various temperatures (40, 50, and 60 °C) and concentrations (0.5% and 2%). For each concentration and temperature condition, at least one experimental case was validated against the corresponding numerical prediction. Specifically, we examined the droplet size ratio (L_D/w), as shown in Fig. 6, which compares the experimental measurements to the numerical results. In all tested conditions, the results demonstrated strong agreement: each data point lies near the diagonal line representing numerical (L_D/w) to experimental (L_D/w) to be 1, indicating close alignment between experimental observations and model predictions, except one condition of 0.5% agarose at 60 °C, where numerical simulation underestimates the experimental results. This consistency across conditions supports the accuracy of our model and validates its ability to simulate the droplet formation process in agarose solutions under different temperature and concentration conditions, to a large extent. The model was hence used to investigate the mechanisms of droplet formation in ultra-low-gelling agarose.

In addition to the direct comparison of (L_D/w) between experimental and numerical results, we also validated our results by comparing our experimental images with the data obtained from numerical simulations. We visually validated a total of six conditions which included various agarose concentrations (0.5% and 2%), temperatures (40, 50, 60 °C), and flow rate ratios (0.08–1.21), see Table S4 in supplementary material. The comparison for each of these conditions is shown in Figs. 7(a)–7(r), presenting experimental images, numerical top views, and 3D isometric views at sequential time points (i)–(iii) arranged vertically.

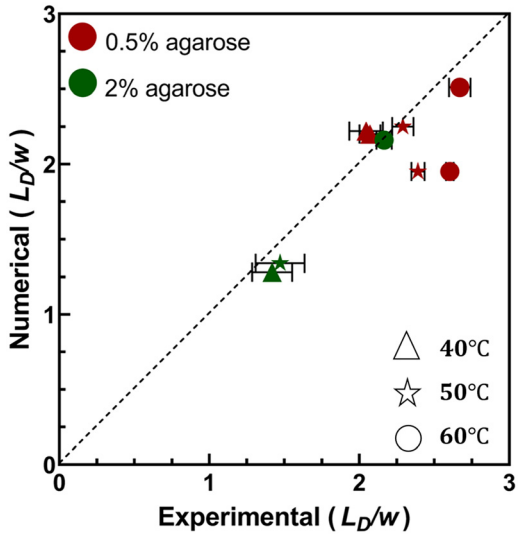

FIG. 6. A comparison of experimental and numerical studies was conducted to validate the effects of agarose gel concentrations (0.5% and 2%) as the discontinuous phase and light mineral oil containing 2% PGPR as the continuous phase. The study examines droplet formation at varied temperatures (40, 50, and 60 °C).

In both experimental and numerical simulations of ultra-low-gelling agarose droplet generation, the interface between the agarose solution and the surrounding continuous phase was observed to exhibit consistent behavior across varying concentrations, temperatures, and flow rates. The droplet formation sequence, including necking and eventual pinch-off, was well-captured, revealing smooth transitions from one regime to the next as shown in Fig. 7. Numerical simulations closely matched these experimental observations, reproducing the interface morphology. The simulated interface consistently showed gradual neck thinning and droplet detachment at time points and shapes comparable to the experimental data. The good agreement between experimental and simulated interfaces validates the robustness of the model, indicating that it can reliably predict interface dynamics under diverse thermal and concentration conditions, crucial for understanding droplet formation in agarose gels.

2. Dynamics of agarose gel droplet formation

We used the numerical model to investigate the dynamics of agarose droplet generation with the help of three parameters that significantly influence the droplet size in the squeezing regime: ϕ, agarose concentration, and temperature. In investigating each of these parameters, we kept the remaining parameters constant.

In the first set of numerical simulations, we demonstrated the effect of flow rate ratio on the droplet formation dynamics. For that, the agarose concentration was maintained at 0.5%, the temperature at 40 °C, and the continuous phase flow rate Qc = 5 μl/min, while varying ϕ. Figure 8(a) illustrates that an increase in ϕ leads to an increase in the numerically predicted droplet size, which aligns well with the experimental observation. The insets of Fig. 8(a) show the snapshots from numerical simulations, showcasing droplet generation for various values of ϕ.

In a typical microfluidic T-junction droplet generator, droplet formation occurs in five primary stages: filling, necking, pinching, threading, and breakup. In the filling stage, the dispersed phase starts to fill the main channel up to a maximum distance h_{fill}, and there is a circular segment at the back of the filled region of the dispersed phase [Fig. 8(b-i)]. As the dispersed phase continues to grow inside the main channel, the continuous phase pushes the dispersed phase and as a result, the neck of the dispersed phase starts to shrink. The diameter of the neck region is denoted by d_{neck} [Fig. 8(b-ii)]. In the squeezing regime, the pressure difference across the phases gradually builds up due to the continued interaction of the two phases, and the pinching off starts to arise [Fig. 8(b-iii)]. After a critical pinching thickness is achieved, the droplet detaches from the dispersed phase [Fig. 8(b-v)]. In the present study, with the dispersed phase being non-Newtonian, an additional threading stage is observed, during which droplet formation is delayed due to the development of narrow threads or filaments that connect the emerging droplet to the supply stream.[53–55] These filaments, extending over a length, l_{thread}, exhibit exponential self-thinning, evolving into nearly uniform cylindrical structures that progressively diminish in diameter until rupture, ultimately leading to droplet breakup at a distance, l_{detach} [Fig. 8(b-iv)]. This behavior is predominantly governed by the rheological properties of the

26 March 2025 12:29:22

© Author(s) 2025

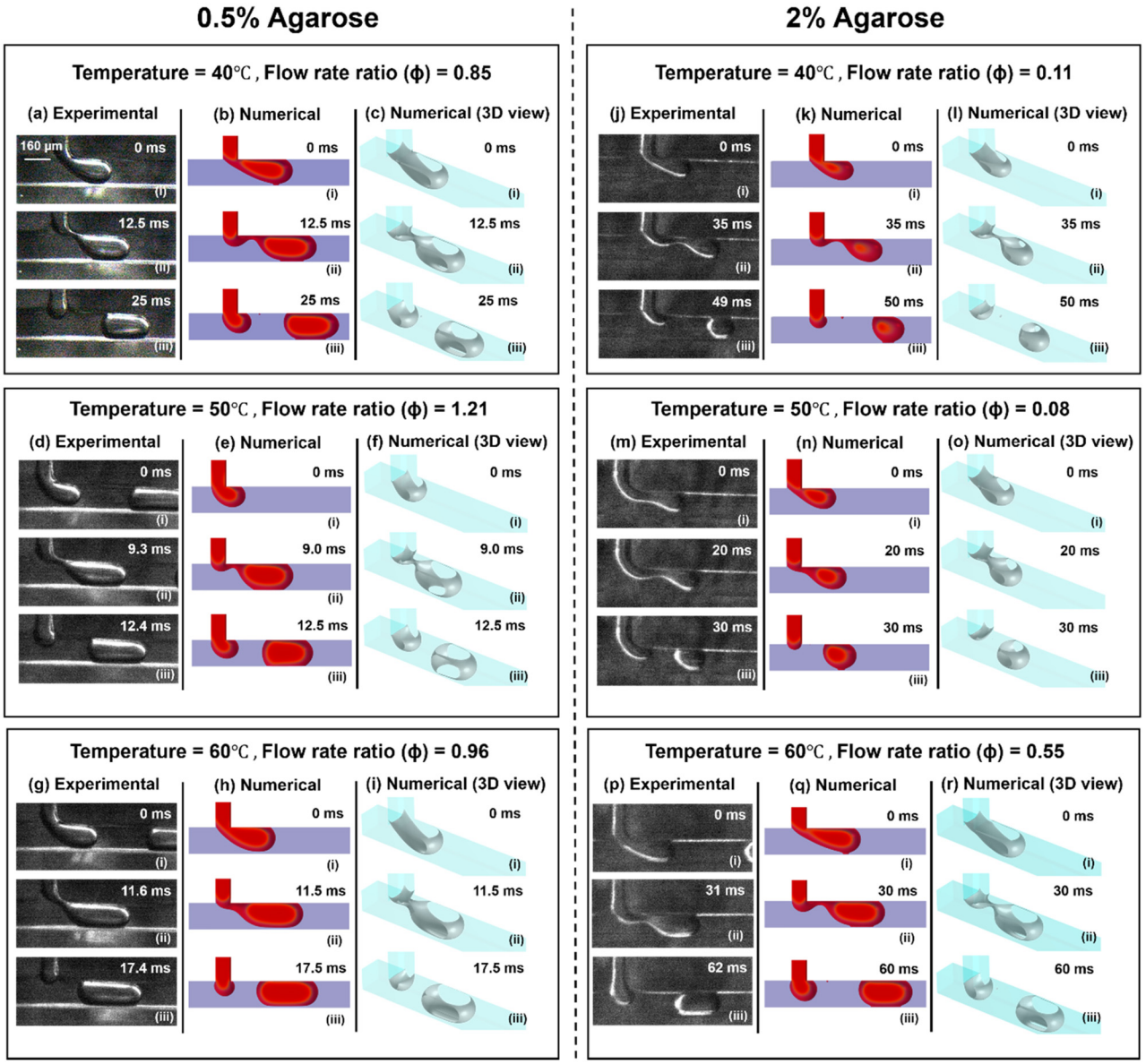

FIG. 7. Visual comparison of experimental and 3D numerical studies for the three critical steps (filling, pinching, and breakup) in droplet generation with varying agarose concentrations (0.5% and 2%), temperatures (40, 50, and 60 °C), and flow rate ratios (ϕ). Panels (a)–(c) show 0.5% agarose gel at 40 °C with experimental images, numerical top views, and 3D isometric views at $\phi = 0.85$, followed by sequential time points (i)–(iii) vertically. Panels (d)–(f) and (g)–(i) show similar results for 0.5% agarose at 50 °C ($\phi = 1.21$) and 60 °C ($\phi = 0.96$), respectively. Panels (j)–(r) illustrate 2% agarose gel at 40 °C ($\phi = 0.11$), 50 °C ($\phi = 0.08$), and 60 °C ($\phi = 0.55$).

non-Newtonian fluid, including elasticity, viscoelasticity, and shear-thinning characteristics.

Figures 8(c) and 8(d) shows the effect of ϕ in governing the droplet formation dynamics. We simulated the two-phase system by keeping $Q_c = 5$ μl/min and varying the Q_d to vary ϕ. We take $\mu_c = 0.015$, $\mu_{d0} = 0.15$ Pa s, and $n = 0.45$. All other parameters are kept unaltered for these investigations. We observe that with increasing ϕ, the droplet formation process accelerates which is attributed to the increase in total flow rate. In addition, an increase in ϕ results in increased droplet size due to increased dispersed phase velocity compared to the continuous phase. Moreover, the dynamics in the filling stage are quite similar for both scenarios. However, in the necking stage, the dispersed phase penetrates a longer distance in the main channel creating a more elongated neck at a higher flow rate ratio. At $\phi = 0.1$, the pinching occurs at the T-junction point, whereas at $\phi = 1$ the pinching is observed at a farther distance (70 μm) from the junction. The pressure inside the agarose phase is observed to be higher than the oil phase and at the pinching region, it reaches a maximum [Figs. 8(c-iv) and

26 March 2025 12:29:22

© Author(s) 2025

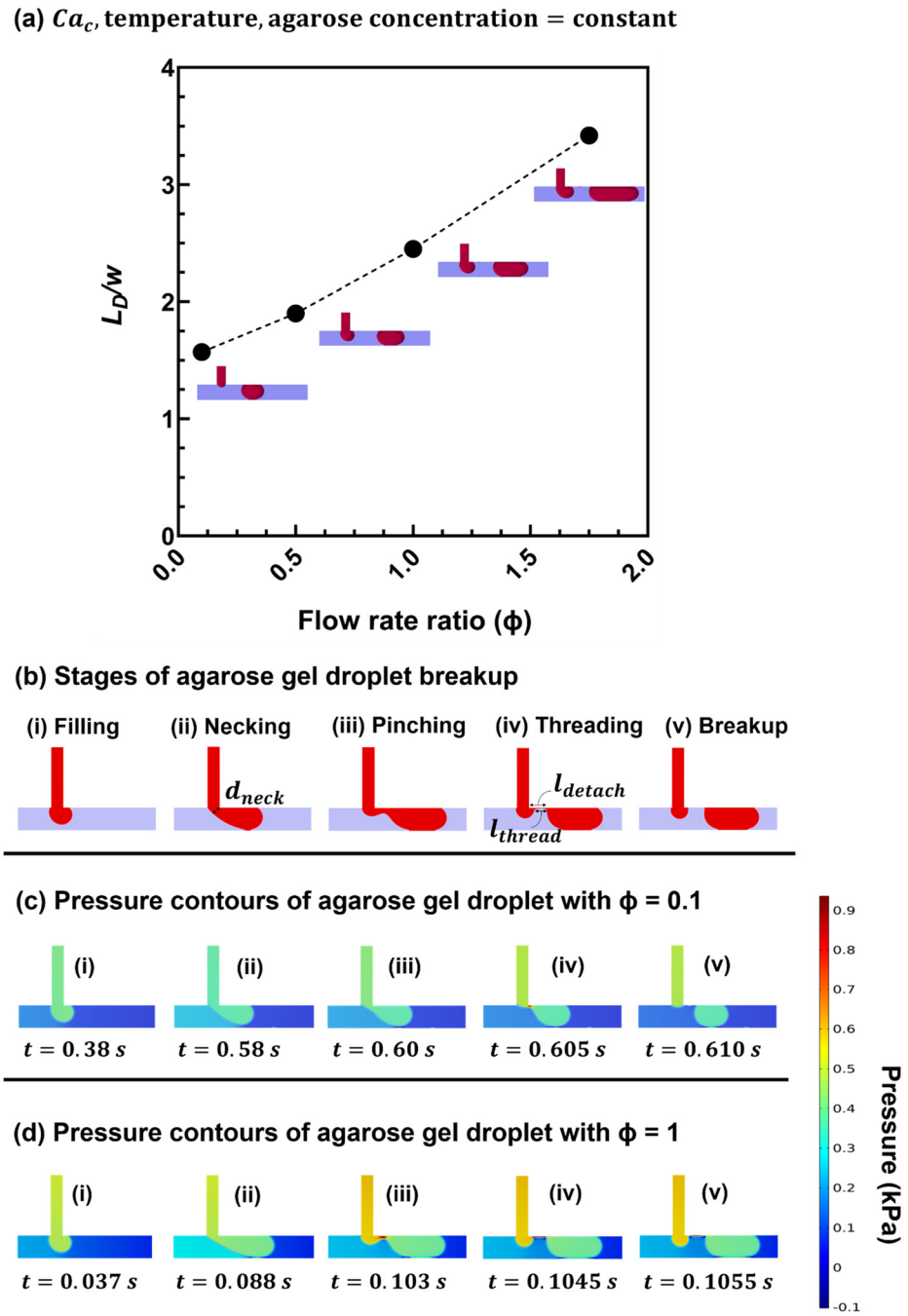

FIG. 8. (a) Numerical study examining the effect of varying ϕ values (from 0.1 to 1.75) on droplet size, with constant Ca_c, temperature, and agarose concentration. The insets display images illustrating droplet sizes at different ϕ values. (b) Numerical simulation depicting the stages of non-Newtonian agarose gel droplet formation, including filling, necking, pinching, threading, and breakup. (c) and (d) Pressure contour maps illustrating the stages of agarose gel droplet formation for ϕ values of 0.1 and 1, respectively. The two-phase interface is distinctly shown by a magenta-colored line for improved visualization.

8(d-iii)]. At a low flow rate ratio ($\phi = 0.1$), the threading region is not present ($l_{thread} \approx 0$), and with increasing ϕ, it appears and is observed to grow ($l_{thread} = 92\ \mu$m for $\phi = 1$). As a consequence, at higher ϕ, the droplet detachment occurs at a relatively far distance from the T-junction. For instance, the droplet detaches immediately after the T-junction at $\phi = 0.1$, whereas at $\phi = 1$, the detachment occurs at $l_{detach} = 145\ \mu$m.

Next, we presented the impact of agarose concentration and temperature on the droplet generation dynamics. Figure 9 shows the numerical simulation results for the droplet generation at 0.5% and 2.0% agarose concentration at 40 and 60 °C. The flow rate ratio is kept constant at $\phi = 1$ considering $Q_c = Q_d = 5\ \mu$l/min. The complex interplay of agarose concentration and temperature of agarose and oil governs the dynamics of the agarose droplet formation resulting in

26 March 2025 12:29:22

© Author(s) 2025

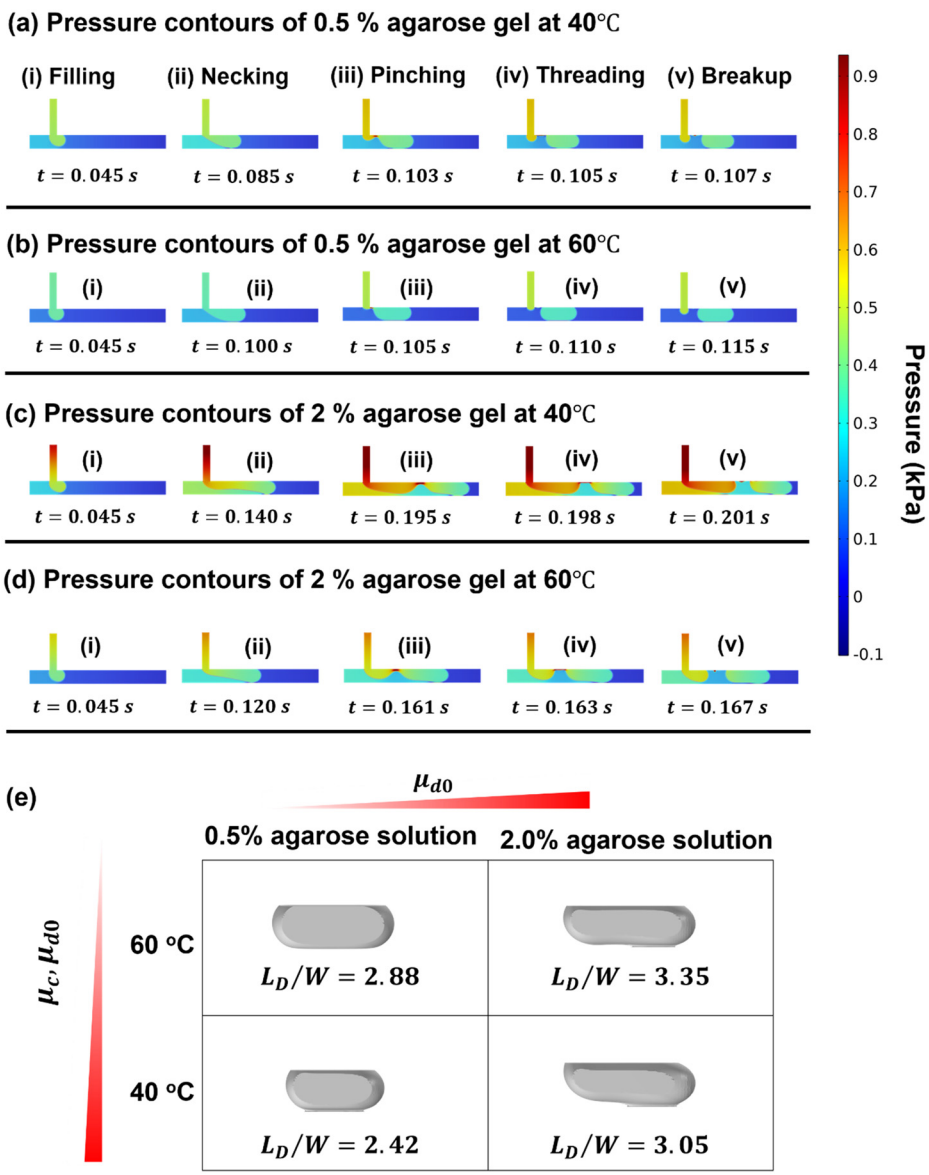

FIG. 9. (a)–(d) Top view of the numerical simulation with different stages of droplet breakup for examining the effect of varying agarose concentration and temperature values on droplet size, with constant Ca_c, and ϕ. The two-phase interface is distinctly shown by a magenta-colored line for improved visualization. (a) At 40 °C and 0.5% agarose concentration. (b) At 60 °C and 0.5% agarose concentration. (c) At 40 °C and 2% agarose concentration. (d) At 60 °C and 2% agarose concentration. (e) The graphical comparisons of the droplet sizes against different temperatures and agarose concentrations show the effect of the interplay between the viscosities of both phases on droplet size.

different droplet sizes for different conditions. We observed that the fluidity of the dispersed phase (agarose solution) strongly influences the pinching-off point and dictates the detachment length. At 40 °C, the droplet detachment occurs at a distance $l_{\text{detach}} = 112\ \mu$m for 0.5% agarose concentration [Fig. 9(a)], whereas the detachment is significantly delayed ($l_{\text{detach}} = 651\ \mu$m) at 2% agarose concentration [Fig. 9(c)]. As temperature increases, both the viscosities of the light mineral oil and the agarose decrease and the rheological behavior of the agarose solutions shifts toward the Newtonian regime from the extreme shear-thinning regime. At 60 °C, the increased fluidity of the agarose solution significantly reduces the droplet detachment distance from the T-junction, in stark contrast to the detachment behavior observed at 40 °C. At 0.5% agarose concentration, detachment occurs almost instantaneously at the T-junction, with $l_{\text{detach}} \approx 0$, whereas at 2% agarose concentration, the detachment length (l_{detach}) extends to ∼355 μm [see Figs. 9(b) and 9(d)]. Moreover, the threading length (l_{detach}) exhibits a positive correlation with the viscous effects of the dispersed phase, while demonstrating an inverse relationship with temperature, similar to the detachment length. Figure 9(e) shows the graphical comparisons of the droplet sizes for different temperatures and agarose concentrations. At higher concentration (2%) and lower temperature (40 °C), the highly viscous agarose solution causes slower droplet breakup, resulting in larger droplets. On the contrary, at higher temperature (60 °C), while the increased fluidity of the agarose solution facilitates the rapid droplet breakup with smaller sizes, the reduced light mineral oil viscosity (44.5% reduction in light mineral oil viscosity at 60 °C compared to its viscosity at 40 °C, see Fig. S1) offers less resistance to the dispersed agarose phase, allowing it to penetrate the

26 March 2025 12:29:22

© Author(s) 2025

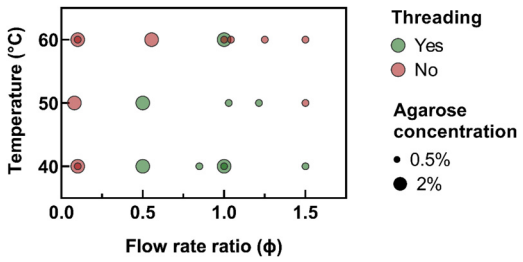

FIG. 10. Regime map depicting the transition between threading and non-threading as a function of ϕ and temperature, for agarose concentrations of 0.5% and 2%.

continuous phase more easily causing an increase in droplet sizes. These counteracting effects generate intermediate sizes of droplets. At 0.5% agarose concentration, the influence of the reduction of light mineral oil viscosity dominates over the increase in agarose fluidity, resulting an increase in droplet size compared to that at 40 °C. On the other hand, at 2% agarose concentration, the agarose viscous effects dominate, causing higher droplet sizes.

Based on the overall numerical simulation results, we conducted a comprehensive analysis of the threading and non-threading droplet breakup with a regime map, focusing on three parameters: ϕ, temperature, and agarose concentration. These parameters are selected based on their significant influence on the droplet generation behavior. Since our study is confined to the small Ca_c range within the squeezing flow regime and experiments showed a weak dependence on Ca_c, we excluded it from our analysis.

As shown in Fig. 10, we identified a clear pattern in the regime transitions. Threading behavior, which indicates significant influences of shear thinning properties of agarose solution on droplet breakup, is predominantly observed at intermediate values of ϕ values and lower temperatures. In contrast, non-threading behavior is more prevalent at lower and higher ϕ values and higher temperatures, where the agarose droplet breakup more closely resembles that of a Newtonian fluid.

IV. CONCLUSIONS

This study focuses on understanding of dynamics of droplet formation in a two-phase microfluidic system where light mineral oil with 2% PGPR is the continuous phase and a non-Newtonian, shear-thinning agarose solution acts as the dispersed phase. We examined the droplet formation process by performing both experiments and simulations, allowing us to study how factors like flow rate ratio ($\phi = Q_d/Q_c$), agarose concentration, Capillary number (Ca_c), and temperature affect the droplet size in the squeezing regime (where $Ca < 0.015$).

Our experimental findings reveal that droplet size, measured as L_D/w, is influenced in different ways by the variables we tested. Specifically, increasing the flow rate ratio (ϕ) causes an increase in droplet size, while the temperature of both phases and concentration of agarose have complex rheological effects on the droplet size. We also found that the effect of the capillary number (Ca_c) is relatively weak in this regime but rather dictates droplet generation regimes. Notably, at an agarose concentration of 0.5%, stable and uniformly sized (monodisperse) droplets could be generated across all tested temperatures (40, 50, and 60 °C). However, when using a higher agarose concentration of 2%, stable droplets were only achieved at the highest temperature of 60 °C due to the increased fluidity of the agarose gel.

To further understand the underlying physics dictating this fluid behavior, we developed a numerical model that we compared with experiments. The model closely matched the experimental results. We numerically showed that the agarose droplet formation process consists of five stages, namely; filling, necking, pinching, threading, and breakup, where threading is an additional stage with a non-Newtonian dispersed phase agarose. We concluded that l_{thread} is directly proportional to ϕ and has a complex relation with agarose concentration, and temperature of both the phases. Through our numerical investigations, we have constructed a regime map delineating the transition between threading and non-threading droplet generation, corresponding to the prevailing conditions.

In summary, this study adds to the understanding of droplet formation with non-Newtonian fluids, such as shear-thinning agarose solutions, which have been studied less than traditional Newtonian systems. Our findings help identify the conditions that allow for stable and uniform droplet formation, thus advancing the knowledge of droplet dynamics in complex fluid systems, which is valuable for applications where precise droplet control is essential.

SUPPLEMENTARY MATERIAL

See the supplementary material for viscosity plots of agarose gel (0.5% and 2%) and light mineral oil with 2% PGPR, their rheological properties used in numerical studies, and the flow rates of dispersed and continuous phases in Fig. 7 for comparing numerical and experimental droplet breakups.

ACKNOWLEDGMENTS

This research has received funding from the European Research Council (ERC) under the European Union's Horizon Europe research and innovation programme (PHOENIX Grant Agreement No. 101043985). We thank U-PRINT Uppsala University's 3D printing facility in the scientific field of medicine and pharmacy for help with mold preparation and we acknowledge Myfab Uppsala for providing facilities and experimental support. Myfab is funded by the Swedish Research Council (No. 2019-00207) as a national research infrastructure.

AUTHOR DECLARATIONS

Conflict of Interest

The authors have no conflicts to disclose.

Author Contributions

Sagar N. Agnihotri and Pradipta Kr. Das contributed equally to this work.

Sagar N. Agnihotri: Conceptualization (equal); Data curation (equal); Formal analysis (equal); Investigation (equal); Methodology (equal); Writing – original draft (equal); Writing – review & editing (equal). **Pradipta Kr. Das:** Data curation (equal); Formal analysis (equal); Investigation (equal); Methodology (equal); Writing – original draft (equal); Writing – review & editing (equal). **Femke Tolboom:** Investigation (supporting); Methodology (supporting); Writing – review & editing (supporting). **Gabriel Werr:** Methodology

26 March 2025 12:29:22

© Author(s) 2025

(supporting); Writing – review & editing (supporting). **Estelle Palierse:** Methodology (supporting); Writing – review & editing (supporting). **Cecilia Persson:** Resources (supporting); Writing – review & editing (supporting). **Maria Tenje:** Conceptualization (equal); Funding acquisition (lead); Resources (lead); Supervision (lead); Writing – original draft (equal); Writing – review & editing (equal).

DATA AVAILABILITY

The data that support the findings of this study are available from the corresponding author upon reasonable request.

REFERENCES

[1]S. N. Agnihotri, M. R. Raveshi, R. Bhardwaj, and A. Neild, "Microvalves for integrated selective droplet generation, splitting and merging on a chip," Microfluid. Nanofluid. **25**(11), 1–13 (2021).
[2]Z. Z. Chong, S. H. Tan, A. M. Gañán-Calvo, S. B. Tor, N. H. Loh, and N. T. Nguyen, "Active droplet generation in microfluidics," Lab Chip **16**(1), 35–58 (2016).
[3]J. H. Jung, G. Destgeer, B. Ha, J. Park, and H. J. Sung, "On-demand droplet splitting using surface acoustic waves," Lab Chip **16**(17), 3235–3243 (2016).
[4]S. N. Agnihotri, M. R. Raveshi, R. Bhardwaj, and A. Neild, "Microfluidic valves for selective on-chip droplet splitting at multiple sites," Langmuir **36**, 1138–1146 (2020).
[5]M. R. Raveshi, S. N. Agnihotri, M. Sesen, R. Bhardwaj, and A. Neild, "Chemical selective droplet splitting using single layer microfluidic valves," Sens. Actuators, B **292**, 233–240 (2019).
[6]S. N. Agnihotri, M. R. Raveshi, R. Bhardwaj, and A. Neild, "Droplet breakup at the entrance to a bypass channel in a microfluidic system," Phys. Rev. Appl. **11**(3), 034020 (2019).
[7]X. Niu, S. Gulati, J. B. Edel, and A. J. Demello, "Pillar-induced droplet merging in microfluidic circuits," Lab Chip **8**(11), 1837–1841 (2008).
[8]C. N. Baroud, M. Robert De Saint Vincent, and J. P. Delville, "An optical toolbox for total control of droplet microfluidics," Lab Chip **7**(8), 1029–1033 (2007).
[9]S. N. Agnihotri, G. S. Ugolini, M. R. Sullivan, Y. Yang, A. De Ganzó, J. W. Lim, and T. Konry, "Droplet microfluidics for functional temporal analysis and cell recovery on demand using microvalves: Application in immunotherapies for cancer," Lab Chip **22**(17), 3258–3267 (2022).
[10]A. Nath, A. Sudeepthi, and A. K. Sen, "Trapping of aqueous droplets under surface acoustic wave-driven streaming in oil-filled microwells," Langmuir **38**(15), 4763–4773 (2022).
[11]P. Garstecki, M. J. Fuerstman, and G. M. H. A. Stone Whitesides, "Formation of droplets and bubbles in a microfluidic T-junction-scaling and mechanism of break-up," Lab Chip **6**(3), 437–446 (2006).
[12]M. R. Raveshi, M. S. Abdul Halim, S. N. Agnihotri, M. K. O'Bryan, A. Neild, and R. Nosrati, "Curvature in the reproductive tract alters sperm–surface interactions," Nat. Commun. **12**(1), 3446 (2021).
[13]M. Tenje, A. Fornell, M. Ohlin, and J. Nilsson, "Particle manipulation methods in droplet microfluidics," Anal. Chem. **90**(3), 1434–1443 (2018).
[14]H. Li, K. Hsieh, P. K. Wong, K. E. Mach, J. C. Liao, and T.-H. Wang, "Single-cell pathogen diagnostics for combating antibiotic resistance," Nat. Rev. Methods Primers **3**(1), 6 (2023).
[15]S. Mashaghi, A. Abbaspourrad, D. A. Weitz, and A. M. van Oijen, "Droplet microfluidics: A tool for biology, chemistry and nanotechnology," TrAC, Trends Anal. Chem. **82**, 118–125 (2016).
[16]L. Y. Yeo, H.-C. Chang, P. P. Y. Chan, and J. R. Friend, "Microfluidic devices for bioapplications," Small **7**(1), 12–48 (2011).
[17]A. B. Theberge, F. Courtois, Y. Schaerli, M. Fischlechner, C. Abell, F. Hollfelder, and W. T. S. Huck, "Microdroplets in microfluidics: An evolving platform for discoveries in chemistry and biology," Angew. Chem., Int. Ed. **49**(34), 5846–5868 (2010).
[18]K. Raj M and S. Chakraborty, "PDMS microfluidics: A mini review," J. Appl. Polym. Sci. **137**(27), 48958 (2020).
[19]Z. Liu, D. Li, X. Wang, Y. Pang, Y. Ma, M. Li, and J. Wang, "Breakup regimes of double emulsion droplets in a microfluidic Y-junction," Phys. Fluids **33**(10), 102009 (2021).
[20]Z. Nie, M. S. Seo, S. Xu, P. C. Lewis, M. Mok, E. Kumacheva, G. M. Whitesides, P. Garstecki, and H. A. Stone, "Emulsification in a microfluidic flow-focusing device: Effect of the viscosities of the liquids," Microfluid. Nanofluid. **5**(5), 585–594 (2008).
[21]C. Cramer, P. Fischer, and E. J. Windhab, "Drop formation in a co-flowing ambient fluid," Chem. Eng. Sci. **59**(15), 3045–3058 (2004).
[22]D. R. Link, E. Grasland-Mongrain, A. Duri, F. Sarrazin, Z. Cheng, G. Cristobal, M. Marquez, and D. A. Weitz, "Electric control of droplets in microfluidic devices," Angew. Chem., Int. Ed. **45**(16), 2556–2560 (2006).
[23]L. Schmid and T. Franke, "SAW-controlled drop size for flow focusing," Lab Chip **13**(9), 1691 (2013).
[24]Y. Huang, P. K. Das, and V. R. Bhethanabotla, "Surface acoustic waves in biosensing applications," Sens. Actuators Rep. **3**, 100041 (2021).
[25]G. P. Zhu, Q. Y. Wang, Z. K. Ma, S. H. Wu, and Y. P. Guo, "Droplet manipulation under a magnetic field: A review," Biosensors **12**(3), 156 (2022).
[26]M. De Menech, P. Garstecki, F. Jousse, and H. A. Stone, "Transition from squeezing to dripping in a microfluidic T-shaped junction," J. Fluid Mech. **595**, 141–161 (2008).
[27]C. N. Baroud, F. Gallaire, and R. Dangla, "Dynamics of microfluidic droplets," Lab Chip **10**(16), 2032–2045 (2010).
[28]R. P. Chhabra and J. F. Richardson, "Chapter 1 - Non-Newtonian fluid behaviour," in *Non-Newtonian Flow and Applied Rheology*, 2nd ed., edited by R. P. Chhabra and J. F. Richardson (Butterworth-Heinemann, Oxford, 2008), pp. 1–55.
[29]R. P. Chhabra and S. A. Patel, *Bubbles, Drops, and Particles in Non-Newtonian Fluids*, 3rd ed. (CRC Press, 2023).
[30]Y. Ding, P. D. Howes, and A. J. Demello, "Recent advances in droplet microfluidics," Anal. Chem. **92**(1), 132–149 (2020).
[31]V. Chokkalingam, B. Weidenhof, M. Krämer, W. F. Maier, S. Herminghaus, and R. Seemann, "Optimized droplet-based microfluidics scheme for sol–gel reactions," Lab Chip **10**(13), 1700–1705 (2010).
[32]L. Yu, M. C. W. Chen, and K. C. Cheung, "Droplet-based microfluidic system for multicellular tumor spheroid formation and anticancer drug testing," Lab Chip **10**(18), 2424–2432 (2010).
[33]P. S. Dittrich and A. Manz, "Lab-on-a-chip: Microfluidics in drug discovery," Nat. Rev. Drug Discov. **5**(3), 210–218 (2006).
[34]Z. Zhu and C. J. Yang, "Hydrogel droplet microfluidics for high-throughput single molecule/cell analysis," Acc. Chem. Res. **50**(1), 22–31 (2017).
[35]B. G. Chung, K.-H. Lee, A. Khademhosseini, and S.-H. Lee, "Microfluidic fabrication of microengineered hydrogels and their application in tissue engineering," Lab Chip **12**(1), 45–59 (2012).
[36]X. Leng, W. Zhang, C. Wang, L. Cui, and C. J. Yang, "Agarose droplet microfluidics for highly parallel and efficient single molecule emulsion PCR," Lab Chip **10**(21), 2841–2843 (2010).
[37]C. Zhang, R. Grossier, N. Candoni, and S. Veesler, "Preparation of alginate hydrogel microparticles by gelation introducing cross-linkers using droplet-based microfluidics: A review of methods," Biomater. Res. **25**(1), 41 (2021).
[38]Y. Wang, T. Cao, J. Ko, Y. Shen, W. Zong, K. Sheng, W. Cao, S. Sun, L. Cai, Y.-L. Zhou, X.-X. Zhang, C. Zong, R. Weissleder, and D. Weitz, "Dissolvable polyacrylamide beads for high-throughput droplet DNA barcoding," Adv. Sci. **7**(8), 1903463 (2020).
[39]H. Wang, H. Liu, H. Liu, W. Su, W. Chen, and J. Qin, "One-step generation of core–shell gelatin methacrylate (GelMA) microgels using a droplet microfluidic system," Adv. Mater. Technol. **4**(6), 1800632 (2019).
[40]T.-D. Dang, Y. H. Kim, H. G. Kim, and G. M. Kim, "Preparation of monodisperse PEG hydrogel microparticles using a microfluidic flow-focusing device," J. Ind. Eng. Chem. **18**(4), 1308–1313 (2012).
[41]S. Hong, H.-J. Hsu, R. Kaunas, and J. Kameoka, "Collagen microsphere production on a chip," Lab Chip **12**(18), 3277–3280 (2012).
[42]E. Chiarello, A. Gupta, G. Mistura, M. Sbragaglia, and M. Pierno, "Droplet breakup driven by shear thinning solutions in a microfluidic T-junction," Phys. Rev. Fluids **2**(12), 123602 (2017).
[43]H. Cao, Y. Lu, L. Wu, C. Zhang, and L.-L. Zhang, "Shear-thinning fluid droplets formation in axisymmetric flow-focusing microfluidics," Ind. Eng. Chem. Res. **63**(8), 3766–3779 (2024).
[44]W. Du, T. Fu, Y. Duan, C. Zhu, Y. Ma, and H. Z. Li, "Breakup dynamics for droplet formation in shear-thinning fluids in a flow-focusing device," Chem. Eng. Sci. **176**, 66–76 (2018).

26 March 2025 12:29:22

© Author(s) 2025

[45]B. Rostami and G. L. Morini, "Generation of Newtonian and non-Newtonian droplets in silicone oil flow by means of a micro cross-junction," Int. J. Multiphase Flow **105**, 202–216 (2018).
[46]A. Khater, O. Abdelrehim, M. Mohammadi, M. Azarmanesh, M. Janmaleki, R. Salahandish, A. Mohamad, and A. Sanati-Nezhad, "Picoliter agar droplet breakup in microfluidics meets microbiology application: Numerical and experimental approaches," Lab Chip **20**(12), 2175–2187 (2020).
[47]N. Naz and Y. Sui, "A three-dimensional level set method for droplet sorting using a non-uniform electric field," Phys. Fluids **35**(8), 082103 (2023).
[48]R. Croce, M. Griebel, and M. A. Schweitzer, "Numerical simulation of bubble and droplet deformation by a level set approach with surface tension in three dimensions," Numer. Methods Fluids **62**(9), 963–993 (2010).
[49]A. Amani, N. Balcázar, J. Castro, and A. Oliva, "Numerical study of droplet deformation in shear flow using a conservative level-set method," Chem. Eng. Sci. **207**, 153–171 (2019).
[50]J. A. Sethian and P. Smereka, "Level set methods for fluid interfaces," Annu. Rev. Fluid Mech. **35**, 341–372 (2003).
[51]M. Romero-Peña, E. K. Ng, and S. Ghosh, "Development of thermally stable coarse water-in-oil emulsions as potential DNA bioreactors," J. Dispersion Sci. Technol. **42**(14), 2075–2084 (2021).
[52]C. A. Stan, S. K. Y. Tang, and G. M. Whitesides, "Independent control of drop size and velocity in microfluidic flow-focusing generators using variable temperature and flow rate," Anal. Chem. **81**(6), 2399–2402 (2009).
[53]P. Kumari and A. Atta, "Non-Newtonian droplet breakup in a T-junction microdevice containing constriction induced asymmetric parallel branches," Phys. Fluids **35**(2), 022004 (2023).
[54]B. Steinhaus, A. Q. Shen, and R. Sureshkumar, "Dynamics of viscoelastic fluid filaments in microfluidic devices," Phys. Fluids **19**(7), 73103 (2007).
[55]G. F. Christopher, S. L. Anna, and J. Rheol, "Passive breakup of viscoelastic droplets and filament self-thinning at a microfluidic T-junction," J. Rheol. **53**(3), 663–683 (2009).

26 March 2025 12:29:22

© Author(s) 2025